Supplementary material:

A Non-local Low-Rank Framework for Ultrasound Speckle Reduction

Anonymous CVPR submission

Paper ID 2395

There are four parts in this supplementary material:

- The first part (part 1) presents the details of the optimization procedure.
- The second part (part 2) presents additional comparison results against state-of-the-art methods.
- The third part (part 3) presents additional despeckled results produced from our method.
- The last part (part 4) presents additional segmentation results with comparison.

Note that all the clinical images presented in this work are obtained from the public ultrasound data set downloaded from the following webpage:
http://www.ultrasoundcases.info.

Part 1. Details of Our Optimization Method

In this part, we present how we iteratively solve (minimize) the low-rank recovery model presented in Eq. 10 of our submitted paper.

Rewriting the Low-rank Recovery Model. First, according to the definition of w_i (see Eq. 7 in our paper), we set w_i to be zero for those smallest singular values, and there are λ of them. Hence, we can re-write the truncated and weighted nuclear norm (TWNN) by skipping the first λ terms in Eq. 7 in the paper as

$$||\Psi_D||_{\tilde{tw}} = \sum_{i=\lambda+1}^{M} w_i \sigma_i(\Psi_D), \tag{1}$$

where Ψ_D is the low-rank component of input Ψ_I (see paper); M is the total number of the singular values of Ψ_D; and w_i is the weight on the i-th singular value σ_i of Ψ_D.

Next, we can devise an alternating direction method of multipliers (ADMM) method to solve our low-rank recovery model (after substituting Eq. 1 above into Eq. 10 in our submitted paper):

$$\min_{\Psi_D, \Psi_\eta} ||\Psi_D||_{\tilde{tw}} + \alpha \sum_{g \in \Psi_\eta} ||g||_\infty + < Y, \Psi_I - \Psi_D - \Psi_\eta > + \beta ||\Psi_I - \Psi_D - \Psi_\eta||_F^2, \tag{2}$$

where $||.||_F$ is the Frobenious norm; α is a parameter set to be 1.0 in the current implementation; g is each 3×3 submatrix in Ψ_η (see paper); Y is the Lagrange multiplier; β is a parameter set to 2; and $< . >$ denotes the inner product. Note that we set the initial values of Ψ_D and Ψ_η as Ψ_I and a zero matrix, respectively, and Y as:

$$Y_0 \ = \ \mathrm{sgn}(\Psi_I) / \max(||\mathrm{sgn}(\Psi_I)||_2, \lambda^{-1} ||\mathrm{sgn}(\Psi_I)||_\infty) \ , \tag{3}$$

where sgn is the sign function; and $||.||_\infty$ denotes the maximum absolute value of all the matrix elements. For details about this initialization, readers may refer to [6, 5].

The core idea of the ADMM is to separate the optimization in Eq. 2 above into two subproblems, and then to solve them iteratively by updating Ψ_D and Ψ_η alternatively.

Subproblem 1: Update $(\Psi_D)_{t+1}$: Given $(\Psi_\eta)_t$ and Y_t, we compute $(\Psi_D)_{t+1}$ by solving (minimizing) the following objective function:

$$\min_{\Psi_D} \sum_{i=\lambda+1}^{M} ||\Psi_D||_{\tilde{tw}} + \frac{\beta}{2}||\Psi_I - \Psi_D - (\Psi_\eta)_t - \frac{1}{\beta}Y_t||_F^2 \; . \tag{4}$$

To solve Eq. 4, we need to expand the nonlinear term $||\Psi_D||_{\tilde{tw}}$. Regarding this, we first prove the following inequality, which is a generalization of Theorem 3.1 in [12]:

To prove: For any given matrix $X \in \mathbb{R}^{m\times n}$, any matrices $A \in \mathbb{R}^{m\times n}$, $B \in \mathbb{R}^{m\times n}$, such that $AA^T = \mathbb{I}$ and $BB^T = \mathbb{I}$, and any diagonal matrix $Q \in \mathbb{R}^{n\times n}$, for non-negative integer $r = rank(A) = rank(B)$ (where $0 \leq r \leq min(m, n)$), we have

$$\text{Tr}(AXQB^T) \leq \sum_{i=1}^{r} \rho_i \sigma_i(X) \; , \tag{5}$$

where $\sigma_i(X)$ is the i-th singular value of X; and ρ_1, ..., ρ_n are diagonal elements in Q.

Proof: We start from the left hand side of Eq. 5:

$$\begin{aligned} \text{Tr}(AXQB^T) &= \text{Tr}(XQB^TA) \quad (\text{by trace rule: } \text{Tr}(M_1M_2) = \text{Tr}(M_2M_1)) \\ &\leq |\text{Tr}(XQB^TA)| \quad (\text{since } x \leq |x| \text{ for any scalar } x) \\ &\leq \sum_{i=1}^{min(m,n)} \sigma_i(X)\sigma_i(QB^TA) \quad (\text{by Von Neumann's trace inequality [9]}) \end{aligned} \tag{6}$$

By singular value decomposition, we know that the non-zero singular values of a matrix (say M) are the square roots of the non-zero eigenvalues of MM^*, where M^* denotes conjugate transpose. Since QB^TA is a real matrix, $(QB^TA)^*$ is just $(QB^TA)^T$.

Let q be the rank of matrix QB^TA, where $q \leq r$. The nonzero $\sigma_i(QB^TA)$ values are the square roots of the non-zero eigenvalues of $(QB^TA)(QB^TA)^T$, which is $QB^TAA^TBQ^T$. Since $AA^T = \mathbb{I}$ and $BB^T = \mathbb{I}$, $QB^TAA^TBQ^T$ is simply a diagonal matrix whose elements are ρ_1^2, ..., ρ_n^2. As a result, the nonzero $\sigma_i(QB^TA)$'s are ρ_1, ..., ρ_q (for $i \in [1, q]$), and the rest ($[q + 1, n]$) are zeros.

Therefore, putting this result into Eq. 6, we can obtain

$$\begin{aligned}\mathrm{Tr}(AXQB^T) &\le \sum_{i=1}^{min(m,n)} \sigma_i(X)\sigma_i(QB^TA) \quad (\text{from } Eq.\ 6)\\ &= \sum_{i=1}^{q}\sigma_i(X)\sigma_i(QB^TA) + \sum_{i=q+1}^{min(m,n)} \sigma_i(X)\sigma_i(QB^TA)\\ &= \sum_{i=1}^{q}\sigma_i(X)\rho_i + \sum_{i=q+1}^{min(m,n)} \sigma_i(X)\cdot 0\\ &\le \sum_{i=1}^{r}\sigma_i(X)\rho_i \quad (\text{since } q \le r \text{ and } \rho_i \ge 0)\ .\end{aligned} \tag{7}$$

This proves Eq. 5. Moreover, following [12], $\mathrm{Tr}(AXQB^T)$ attains maximum when

$$A = (\sqrt{\rho_1}u_1, \ldots, \sqrt{\rho_r}u_r, \mathbf{0})^T \text{ and } B = (\sqrt{\rho_1}v_1, \ldots, \sqrt{\rho_r}v_r, \mathbf{0})^T. \tag{8}$$

where $U_1\Sigma_1V_1$ is the singular value decomposition (SVD) of X; $U_1 = (u_1, \ldots, u_{min(m,n)})$; $V_1 = (v_1, \ldots, v_{min(m,n)})$; and Σ_1 is a diagonal matrix [End of Proof].

By setting X as Ψ_D amd ρ_i in Q as

$$\rho_i = \frac{\theta\sqrt{K+1}}{\sqrt{\sigma_i(\Psi_D)} + \varepsilon}\ , \tag{9}$$

where θ, K and ε are defined in paper, we can employ Eq. 5 and rewrite TWNN of Eq. 1 as:

$$\begin{aligned}||\Psi_D||_{\tilde{tw}} &= \sum_{i=\lambda+1}^{M} w_i\sigma_i(\Psi_D) \quad (\text{by } Eq.\ 1)\\ &= \sum_{i=1}^{M}\rho_i\sigma_i(\Psi_D) - \sum_{i=1}^{\lambda}\rho_i\sigma_i(\Psi_D)\\ &\approx \sum_{i=1}^{M}\rho_i\sigma_i(\Psi_D) - \max_{AA^T=\mathbb{I}, BB^T=\mathbb{I}} \mathrm{Tr}(A\Psi_D QB^T), \quad (\text{by } Eq.\ 5)\end{aligned} \tag{10}$$

From Eq. 7 in paper, $\rho_i = w_i$ when $i \ge \lambda + 1$. By replacing TWNN of Eq. 1 with

Eq. 10, we can reformulate the optimization in Eq. 4 as

$$\min_{\Psi_D} \sum_{i=1}^{M} \rho_i \sigma_i(\Psi_D) - \max_{AA^T=\mathbb{I}, BB^T=\mathbb{I}} \mathrm{Tr}(A\Psi_D Q B^T) + \frac{\beta}{2}||\Psi_I - \Psi_D - (\Psi_\eta)_t - \frac{1}{\beta}Y_t||_F^2. \tag{11}$$

According to [12], we can solve Eq. 11 by an efficient two-step scheme to update Ψ_D, and (A, B) in an iterative manner. In the j-th ($j \in [1, J]$) iteration, the two-step scheme is described as:

Step 1.1 Let Θ_j be $(\Psi_D)_{t+1}$ in the j-th iteration, and $[(U_2)_j (\Sigma_2)_j (V_2) j] = \mathrm{svd}(\Theta_j)$, where $(U_2)_j = (u_1, \dots, u_M)^T$ and $(V_2)_j = (v_1, \dots, v_M)^T$. Then we can estimate A_j and B_j using the following equation:

$$A_j = (\sqrt{\rho_1}u_1, \dots, \sqrt{\rho_\lambda}u_\lambda, \mathbf{0})^T \text{ and } B_j = (\sqrt{\rho_1}v_1, \dots, \sqrt{\rho_\lambda}v_\lambda, \mathbf{0})^T. \tag{12}$$

Step 1.2 After obtaining A_j and B_j in Step 1.1, Θ_{j+1} at the $(j{+}1)$-th iteration is computed as:

$$\min_{\Psi_D} \sum_{i=1}^{M} \rho_i \sigma_i(\Psi_D) - \mathrm{Tr}(A_j \Psi_D Q B_j^T) + \frac{\beta}{2}||\Psi_I - \Psi_D - (\Psi_\eta)_t - \frac{1}{\beta}Y_t||_F^2. \tag{13}$$

Now, we can employ the accelerated proximal gradient line search method (APGL) [12] to minimize Eq. 13 above. Let $f(\Psi_D) = -\mathrm{Tr}(A\Psi_D Q B^T) + \frac{\beta}{2}||\Psi_I - \Psi_D - (\Psi_\eta)_t - \frac{1}{\beta}Y_t||_F^2$, and $e(\Psi_D) = \sum_{i=1}^{M} \rho_i \sigma_i(\Psi_D)$. For a given paramter $s > 0$, by introducing an auxiliary variable Z, APGL method constructs an approximation of Eq. 13 as:

$$Q(\Psi_D, Z) = f(Z) + < \Psi_D - Z, \nabla f(Z) > + \frac{1}{2s}||\Psi_D - Z||_F^2 + e(\Psi_D)\ . \tag{14}$$

Then, APGL method uses another iteration ($k \in [1, K_2]$) to iteratively update Ψ_D, Z and s. The initial value of Z and s are set as Θ_j and 1, respectively. Assuming that Γ_k

is the k-th iteration for computing Θ_{j+1}, Γ_{k+1} in the $(k+1)$-th iteration is computed as:

$$
\begin{aligned}
\Gamma_{k+1} &= arg\min_{\Psi_D} Q(\Psi_D, Z_k) \quad (\text{from } Eq.\ 14) \\
&=< \Psi_D - Z_k, \nabla f(Z_k) > + \frac{1}{2s_k}||\Psi_D - Z_k||_F^2 + g(\Psi_D) \\
&\quad (\text{by removing terms with } Z_k \text{ from } Eq.\ 14) \\
&= arg\min_{\Psi_D} \frac{1}{2s_k}||\Psi_D - (Z_k - s_k \nabla f(Z_k))||_F^2 + \sum_{i=1}^{M} \rho_i \sigma_i(\Psi_D) \qquad (15) \\
&\quad \left(\text{by adding } \frac{s_k(\nabla f(Z_k))^2}{2}\right) \\
&= arg\min_{\Psi_D} \frac{1}{2s_k}||\Psi_D - \Re_k||_F^2 + \sum_{i=1}^{M} \rho_i \sigma_i(\Psi_D)\ , \quad (\text{by calculating } \nabla f(Z_k))
\end{aligned}
$$

where $\Re_k = Z_k + s_k(A_j^T B_j Q^T - \frac{\beta}{2}(\Psi_I - (\Psi_\eta)_t - \frac{1}{\beta}Y_t))$. Now, according to [3], the closed-formed solution of Eq. 15 is given by:

$$
\begin{cases}
(U_3, \Sigma_3, V_3) = \text{svd}(\Re_k) \\
(\Gamma)_{k+1} = U_3(\Omega(\Sigma_3))V_3^T\ ,
\end{cases} \qquad (16)
$$

where the singular value shrinkage operator $\Omega(\Sigma_3)_{ii}$ is:

$$
\Omega(\Sigma_3)_{ii} = \max(\Sigma_{ii} - 2\rho_i s_k, 0), \qquad (17)
$$

where Σ_{ii} is the i-th largest singular values in the diagonal matrix Σ_3.

Meanwhile, according to [4] [12], Z_{k+1} and s_{k+1} are computed as:

$$
Z_{k+1} = \Gamma_{k+1} + \frac{s_k - 1}{s_k}(\Gamma_{k+1} - \Gamma_k), \text{ and } s_{k+1} = \frac{1 + \sqrt{1 + 4(s_k)^2}}{2}. \qquad (18)
$$

Subproblem 2: Update $(\Psi_\eta)_{t+1}$: Given $(\Psi_D)_{t+1}$ and Y_t, $(\Psi_\eta)_{t+1}$ is updated by the minimization below:

$$
\min_{\Psi_\eta} \alpha \sum_{g \in \Psi_\eta} ||g||_\infty + \frac{\beta}{2}||\Psi_I - (\Psi_D)_{t+1} - \Psi_\eta - \frac{1}{\beta}Y_t||_F^2\ , \qquad (19)
$$

where α and g are defined in Eq. 10 of our paper. According to [7], the solution of Eq. 19 is the proximal operator related with a structured sparsity-inducing norm,

Algorithm 1 Our ADMM procedure to recover Ψ_D from Ψ_I

Input: a patch group matrix Ψ_I from input image
1: **for** t=0:T **do**
2: **for** j=0:J **do**
3: compute A_j and B_j using Eq. 12
4: **for** k=0:K_2 **do**
5: update Γ_{k+1} using Eq. 16
6: update Z_{k+1} and s_{k+1} using Eq. 18
7: **end for**
8: **end for**
9: compute $(\Psi_\eta)_{t+1}$ by solving Eq. 19 using the method proposed in [7]
10: $Y_{t+1} = Y_t + \rho(\Psi_I - (\Psi_D)_{t+1} - (\Psi_\eta)_{t+1})$
11: **end for**
Output: Ψ_D

and it can be exactly computed by solving a quadratic min-cost flow problem [7] in polynomial time. Algorithm 1 summaries the whole procedure for the low-rank matrix recovery. For all the experiments, we empirically set both J and K_2 as 2, and T as [3, 10], with a large T for a high speckle noise level in the input ultrasound image.

Part 2. Additional Comparison Results

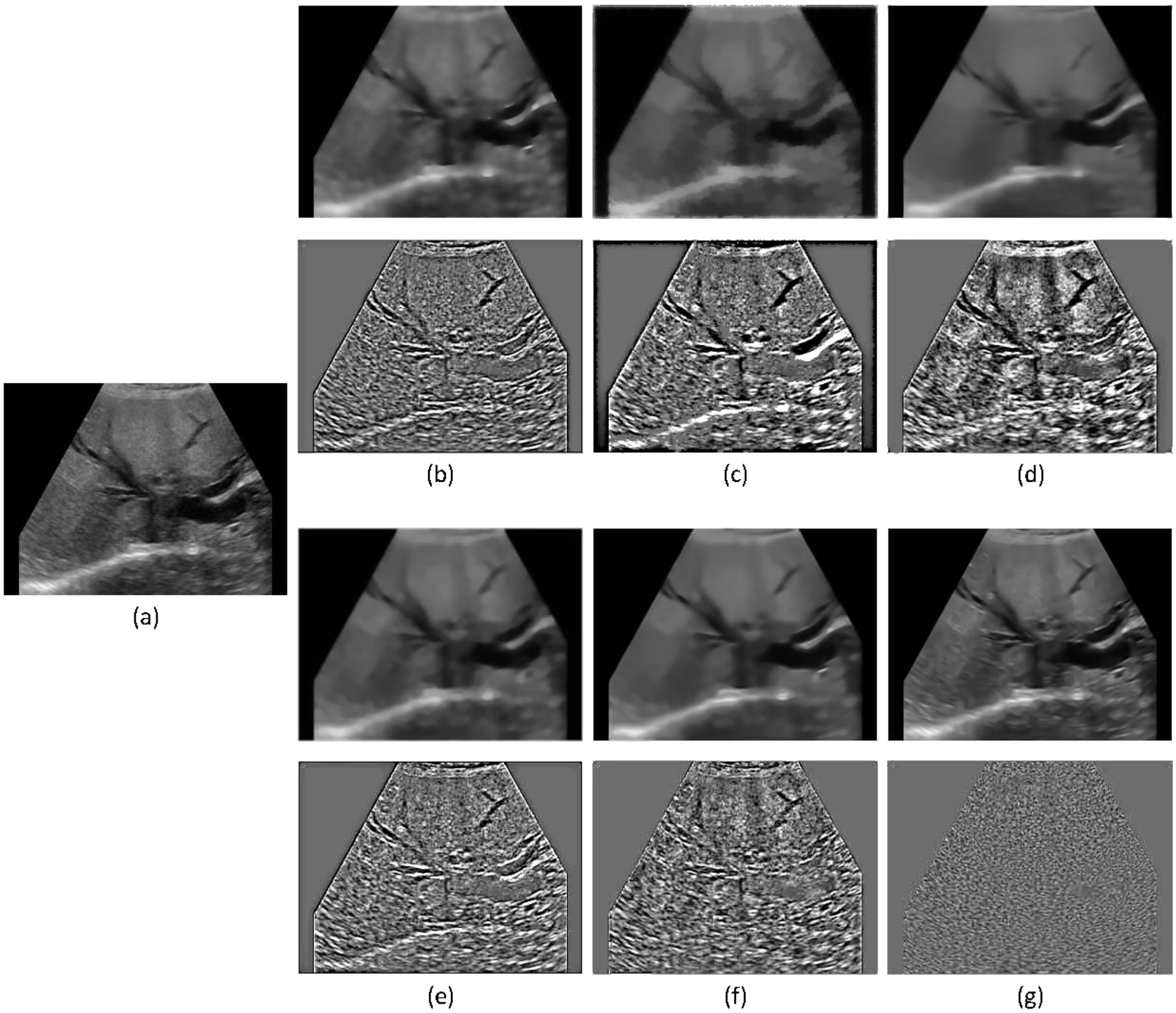

Figure 1: Additional comparison result #1. (a) input clinical ultrasound image with an inhomogeneous mass in the liver hilum. Top row of (b)-(g): despeckled results produced from SRAD [11], SBF [8], OBNLM [1], ADLG [2], NLMLS [10], and our method, respectively. Bottom row of (b)-(g) shows the noise components of these despeckled results.

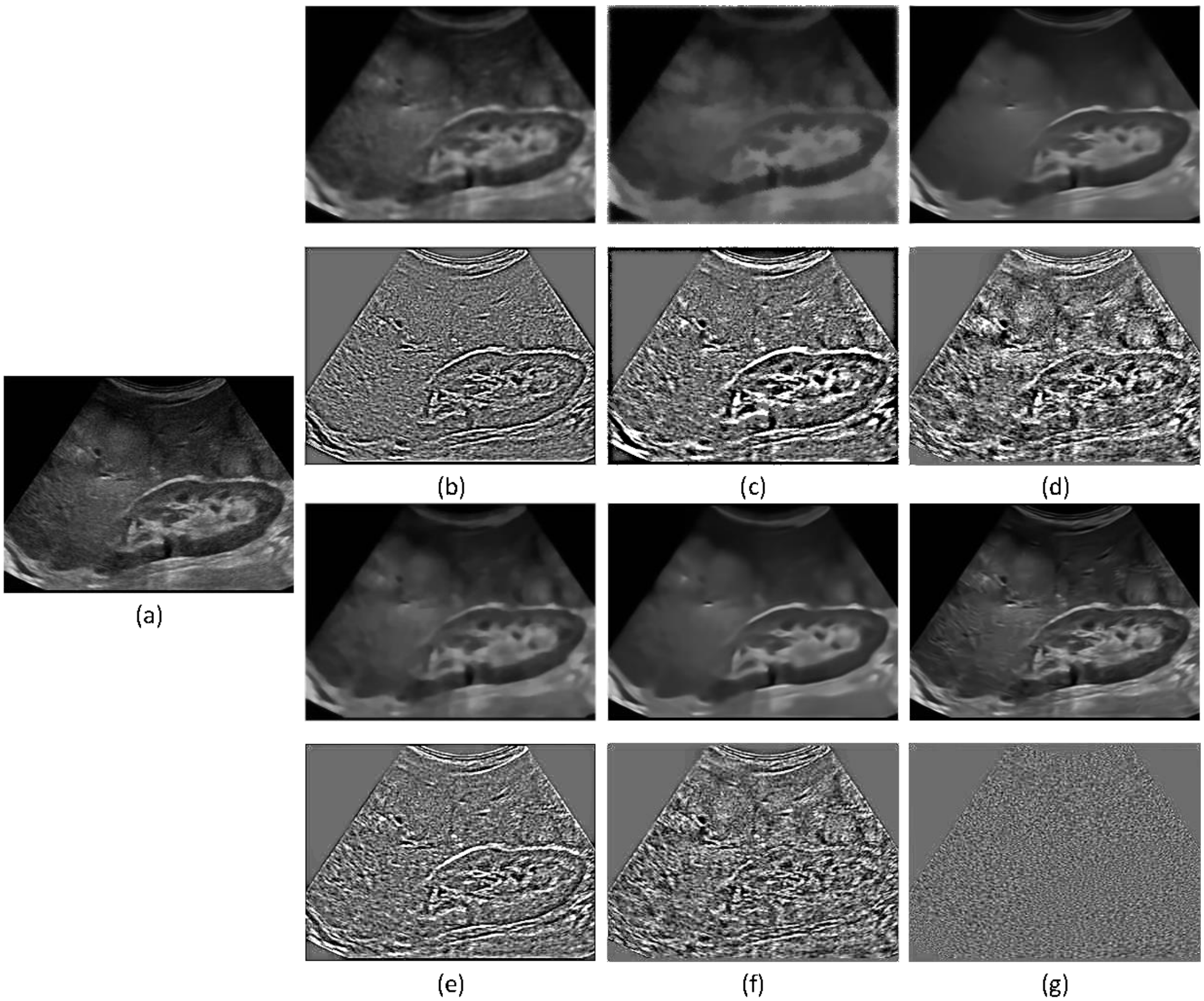

Figure 2: Additional comparison result #2. (a) input clinical ultrasound image with an enlarged hypoechoic inguinal lymph node. Top row of (b)-(g): despeckled results produced from SRAD [11], SBF [8], OBNLM [1], ADLG [2], NLMLS [10], and our method, respectively. Bottom row of (b)-(g) shows the noise components of these despeckled results.

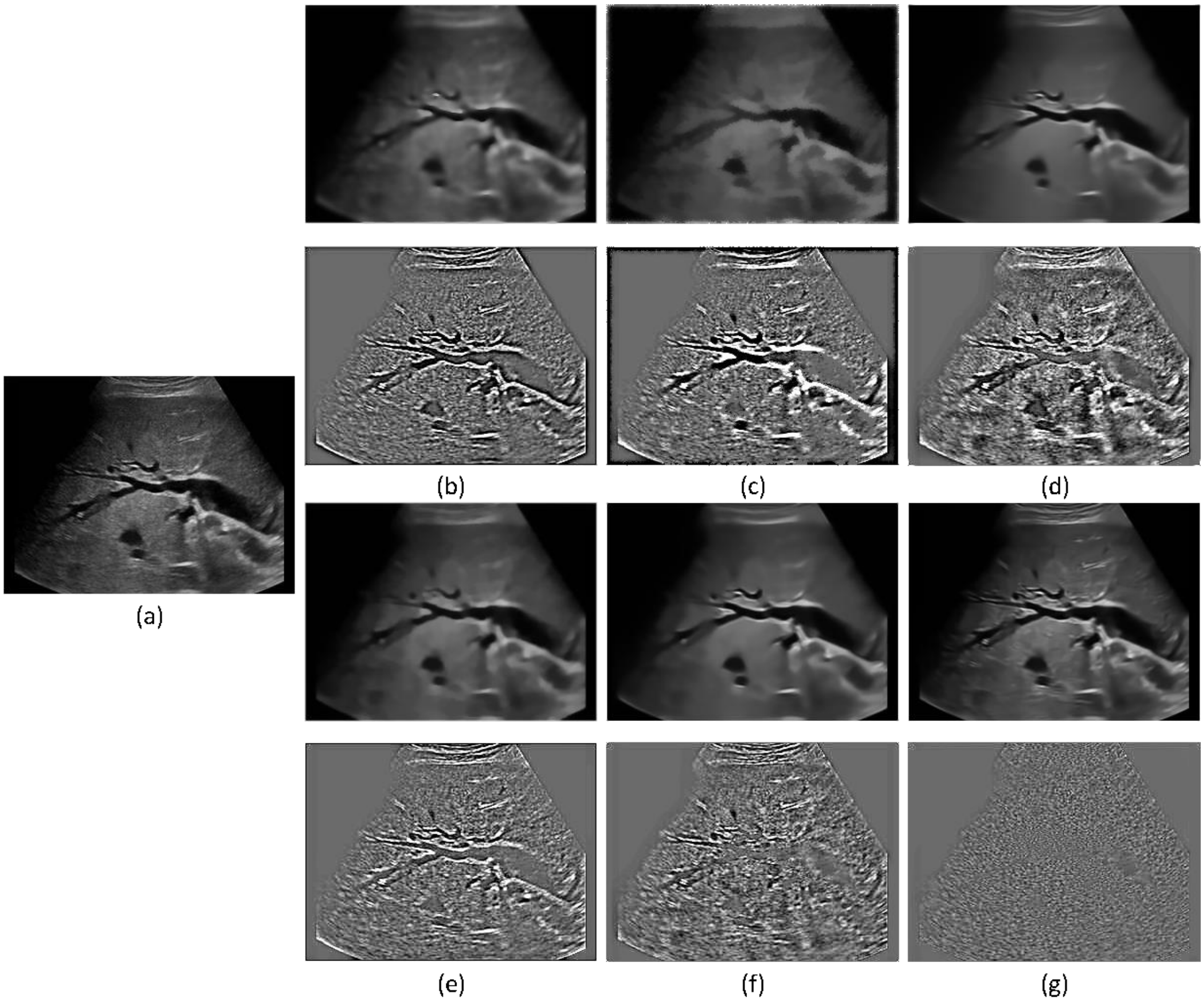

Figure 3: Additional comparison result #3. (a) input clinical ultrasound image with mulitiple common bile duct stones. Top row of (b)-(g): despeckled results produced from SRAD [11], SBF [8], OBNLM [1], ADLG [2], NLMLS [10], and our method, respectively. Bottom row of (b)-(g) shows the noise components of these despeckled results.

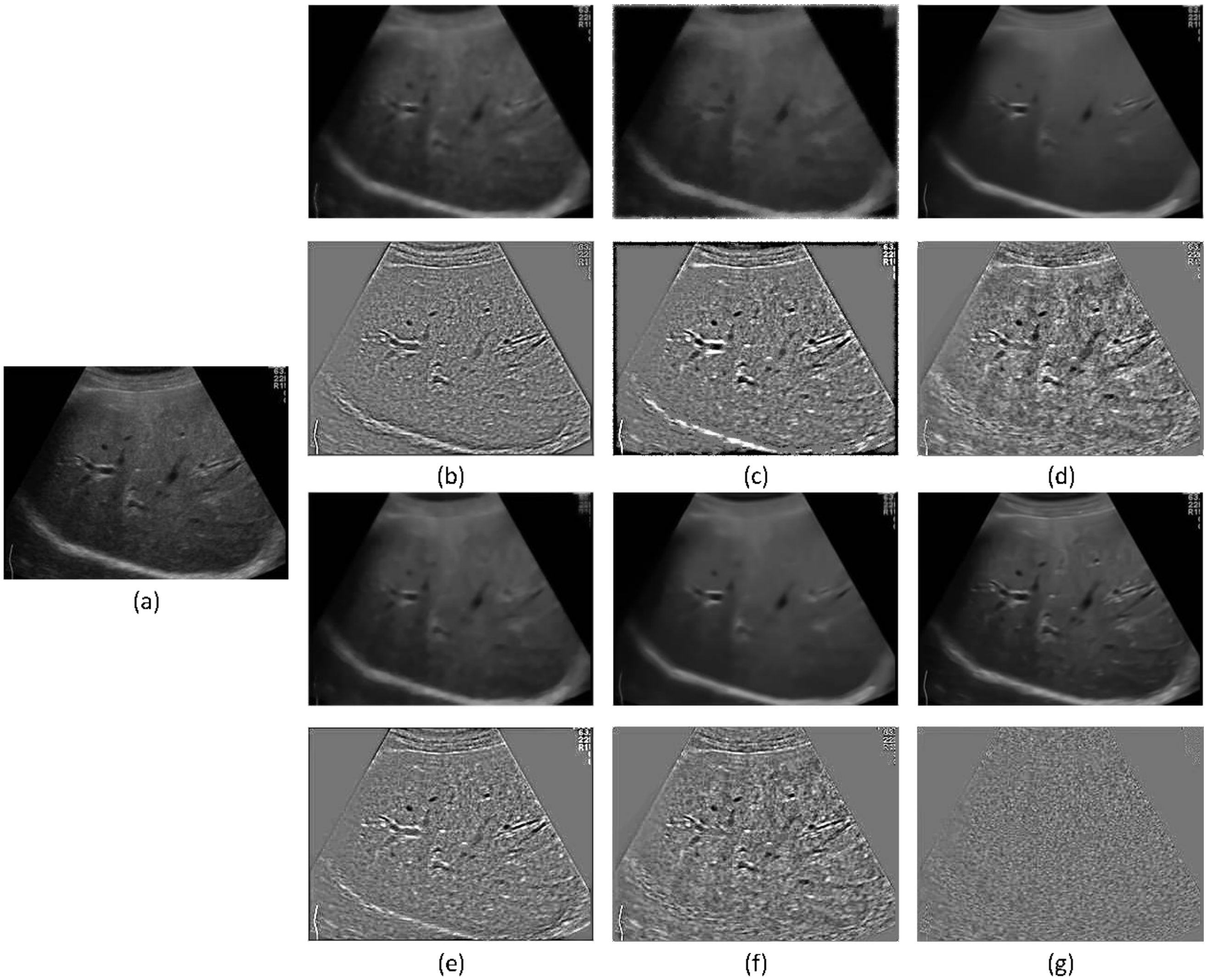

Figure 4: Additional comparison result #4. (a) input clinical ultrasound image with dilatated intrahepatic bile ducts. Top row of (b)-(g): despeckled results produced from SRAD [11], SBF [8], OBNLM [1], ADLG [2], NLMLS [10], and our method, respectively. Bottom row of (b)-(g) shows the noise components of these despeckled results.

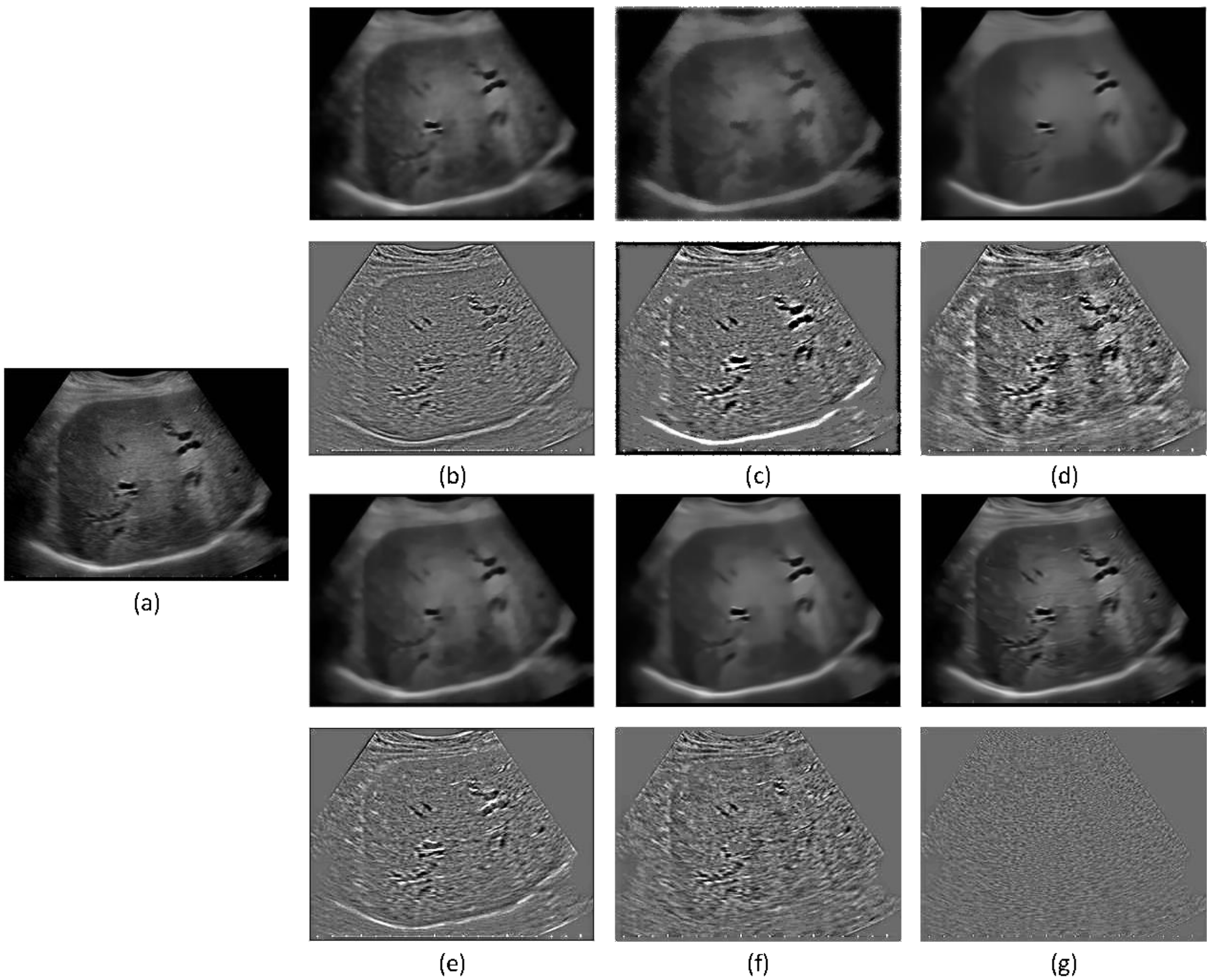

Figure 5: Additional comparison result #5. (a) input clinical ultrasound image with dilatated bile ducts.. Top row of (b)-(g): despeckled results produced from SRAD [11], SBF [8], OBNLM [1], ADLG [2], NLMLS [10], and our method, respectively. Bottom row of (b)-(g) shows the noise components of these despeckled results.

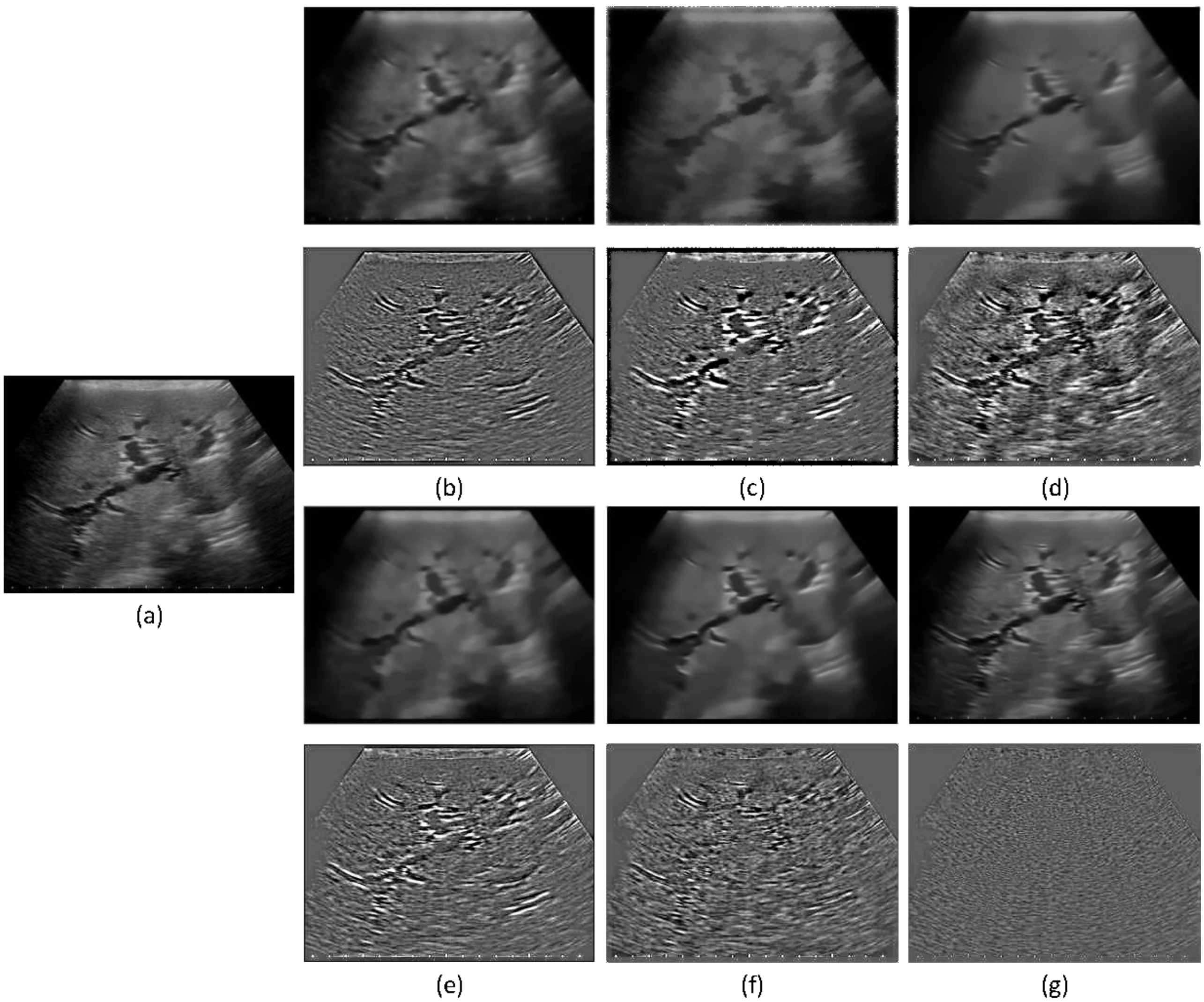

Figure 6: Additional comparison result #6. (a) input clinical ultrasound image with dilatated bile ducts. Top row of (b)-(g): despeckled results produced from SRAD [11], SBF [8], OBNLM [1], ADLG [2], NLMLS [10], and our method, respectively. Bottom row of (b)-(g) shows the noise components of these despeckled results.

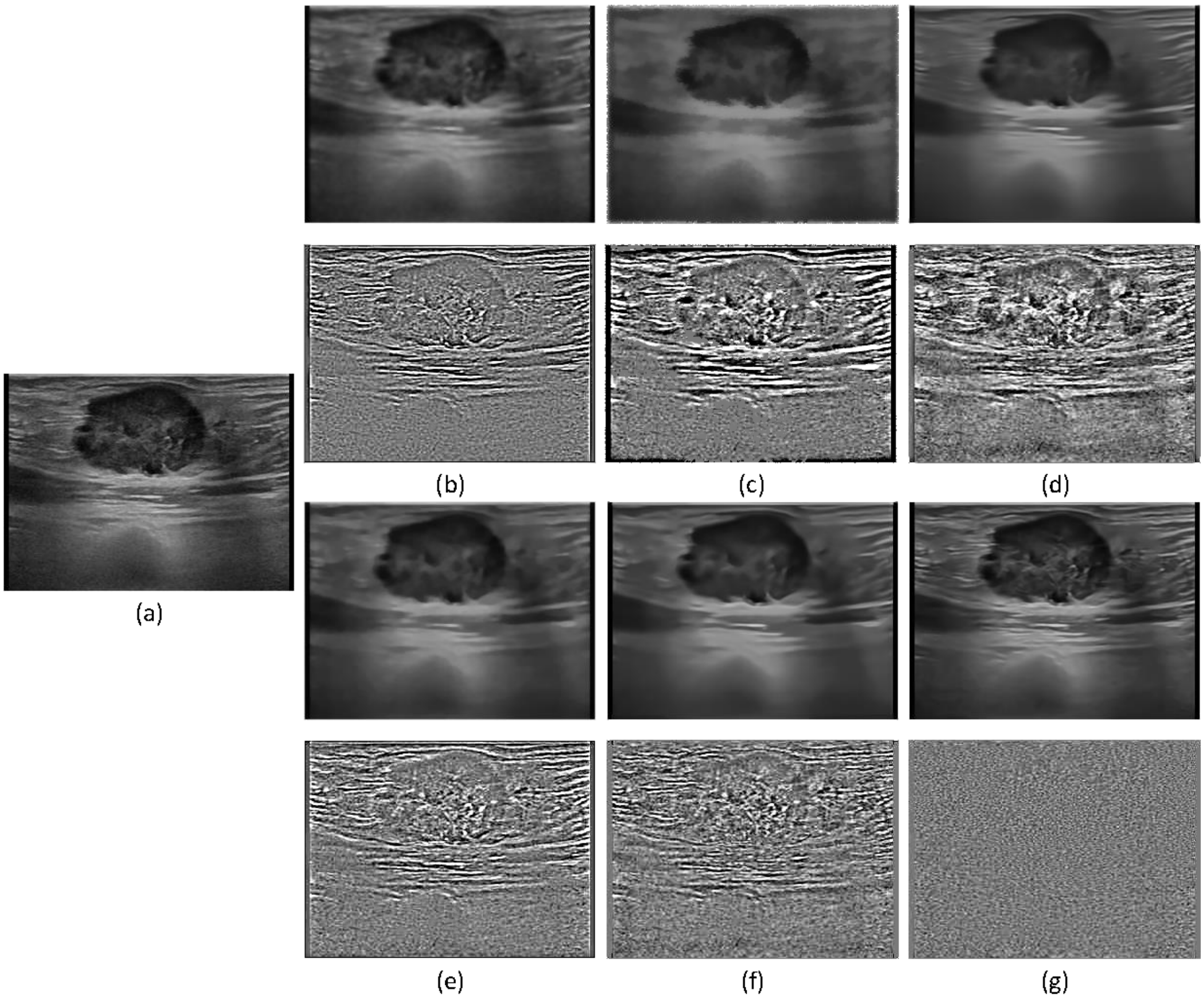

Figure 7: Additional comparison result #7. (a) input clinical ultrasound image with an enlarged hypoechoic inguinal lymph node. Top row of (b)-(g): despeckled results produced from SRAD [11], SBF [8], OBNLM [1], ADLG [2], NLMLS [10], and our method, respectively. Bottom row of (b)-(g) shows the noise components of these despeckled results.

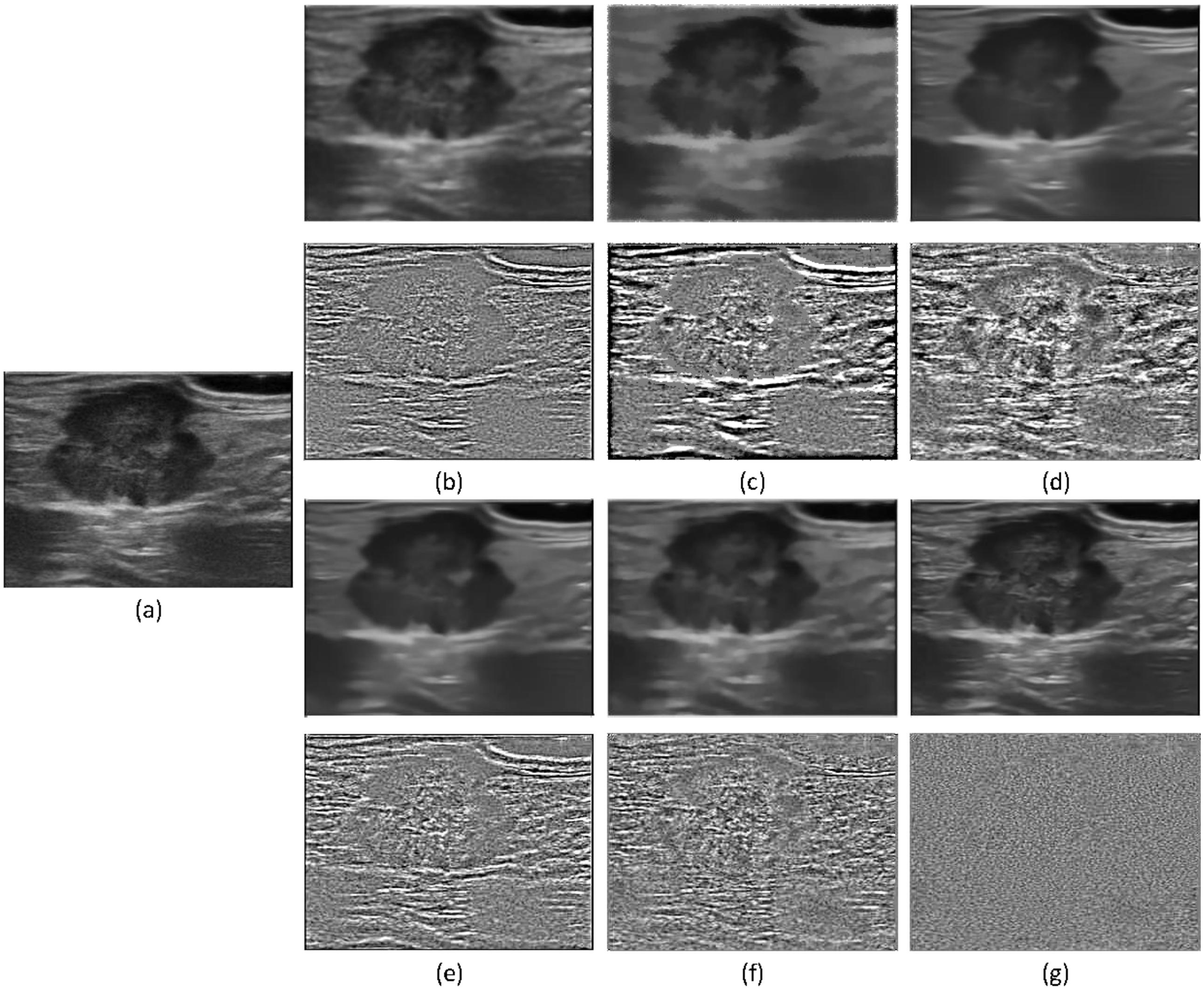

Figure 8: Additional comparison result #8. (a) input clinical ultrasound image with an enlarged hypoechoic inguinal lymph node. Top row of (b)-(g): despeckled results produced from SRAD [11], SBF [8], OBNLM [1], ADLG [2], NLMLS [10], and our method, respectively. Bottom row of (b)-(g) shows the noise components of these despeckled results.

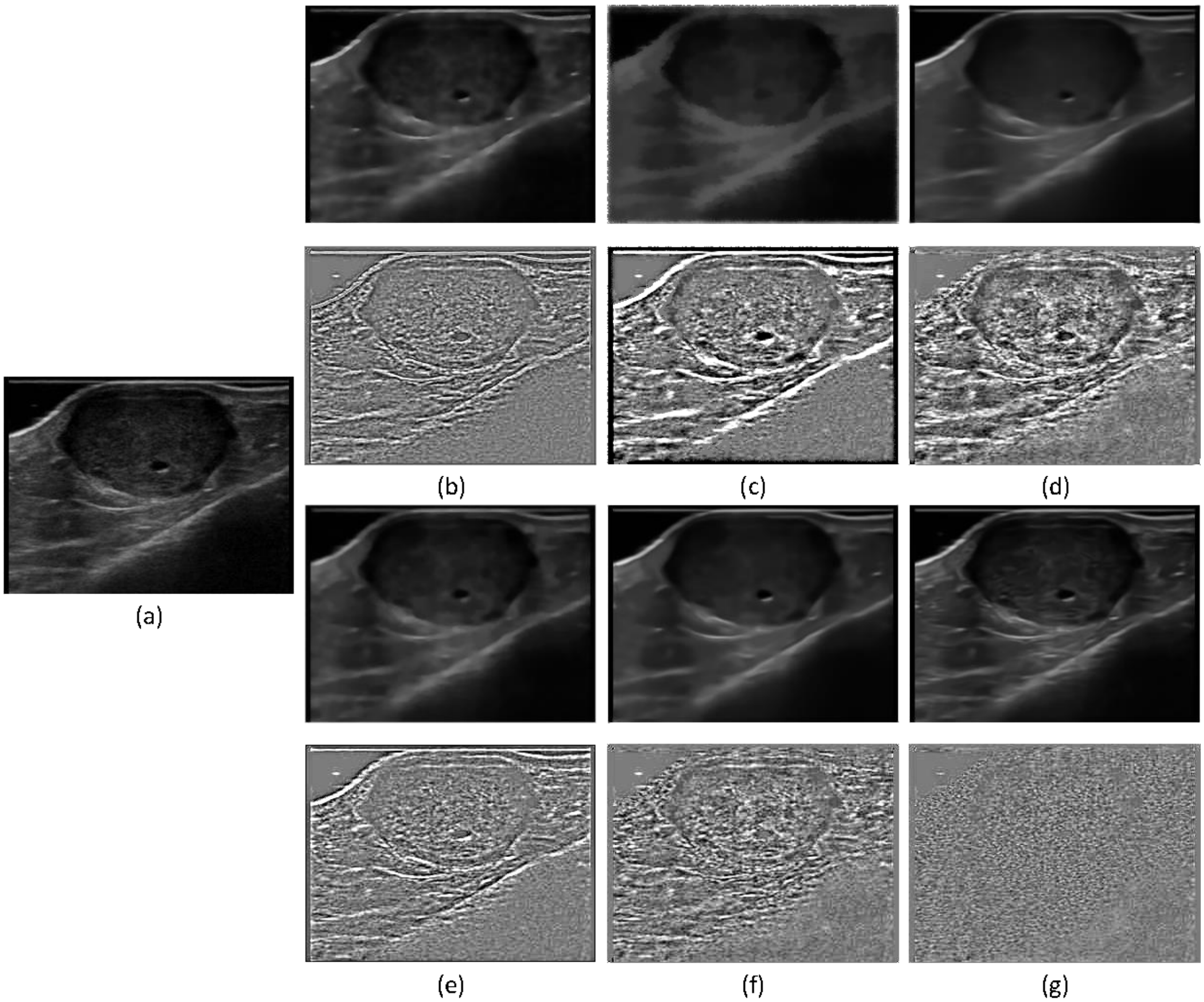

Figure 9: Additional comparison result #9. (a) input clinical ultrasound image with a highly vascularized compressible mass in the lower leg. Top row of (b)-(g): despeckled results produced from SRAD [11], SBF [8], OBNLM [1], ADLG [2], NLMLS [10], and our method, respectively. Bottom row of (b)-(g) shows the noise components of these despeckled results.

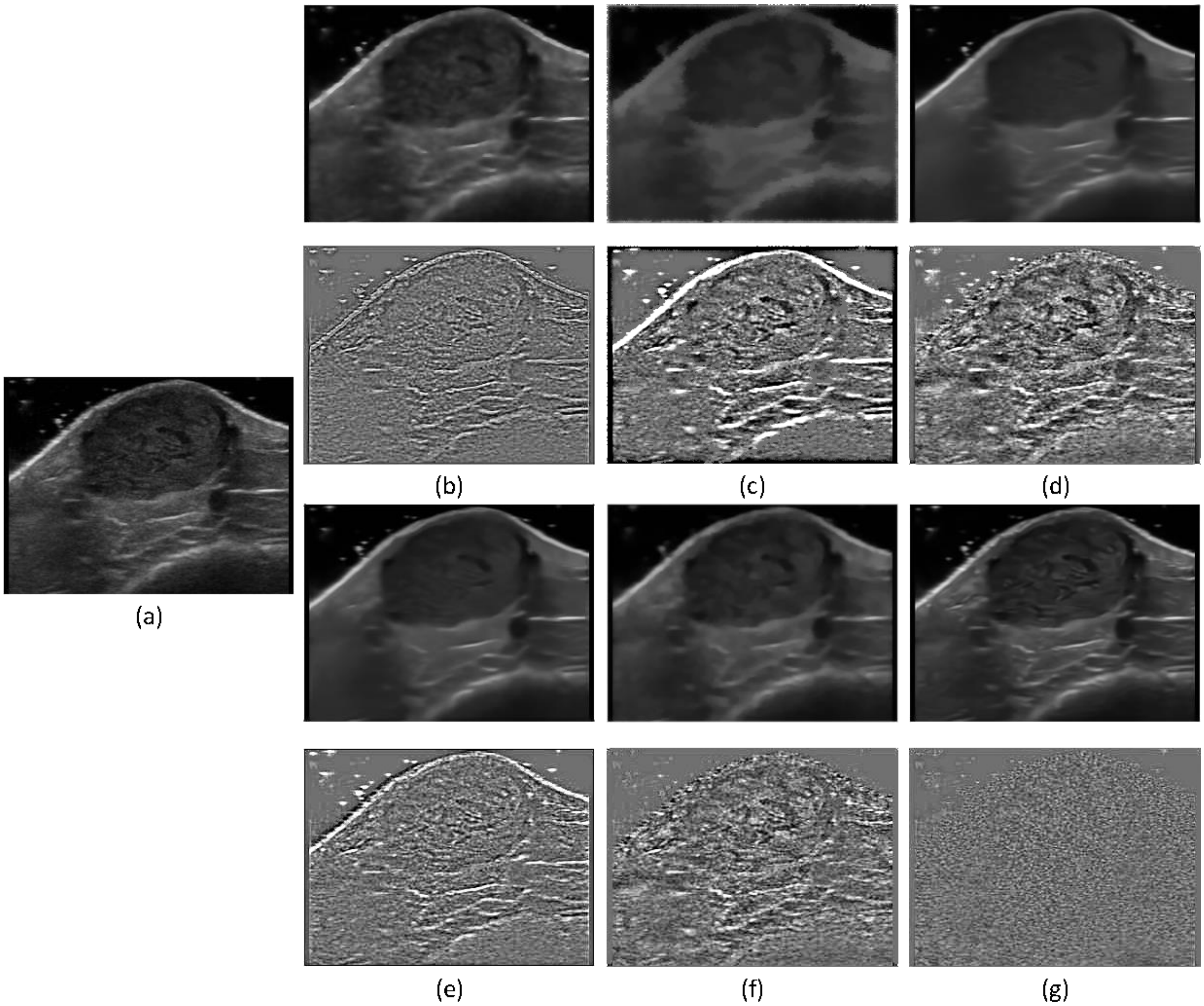

Figure 10: Additional comparison result #10. (a) input clinical ultrasound image with a highly vascularized compressible mass in the lower leg. Top row of (b)-(g): despeckled results produced from SRAD [11], SBF [8], OBNLM [1], ADLG [2], NLMLS [10], and our method, respectively. Bottom row of (b)-(g) shows the noise components of these despeckled results.

Part 3. Additional Ultrasound Speckle Reduction Results

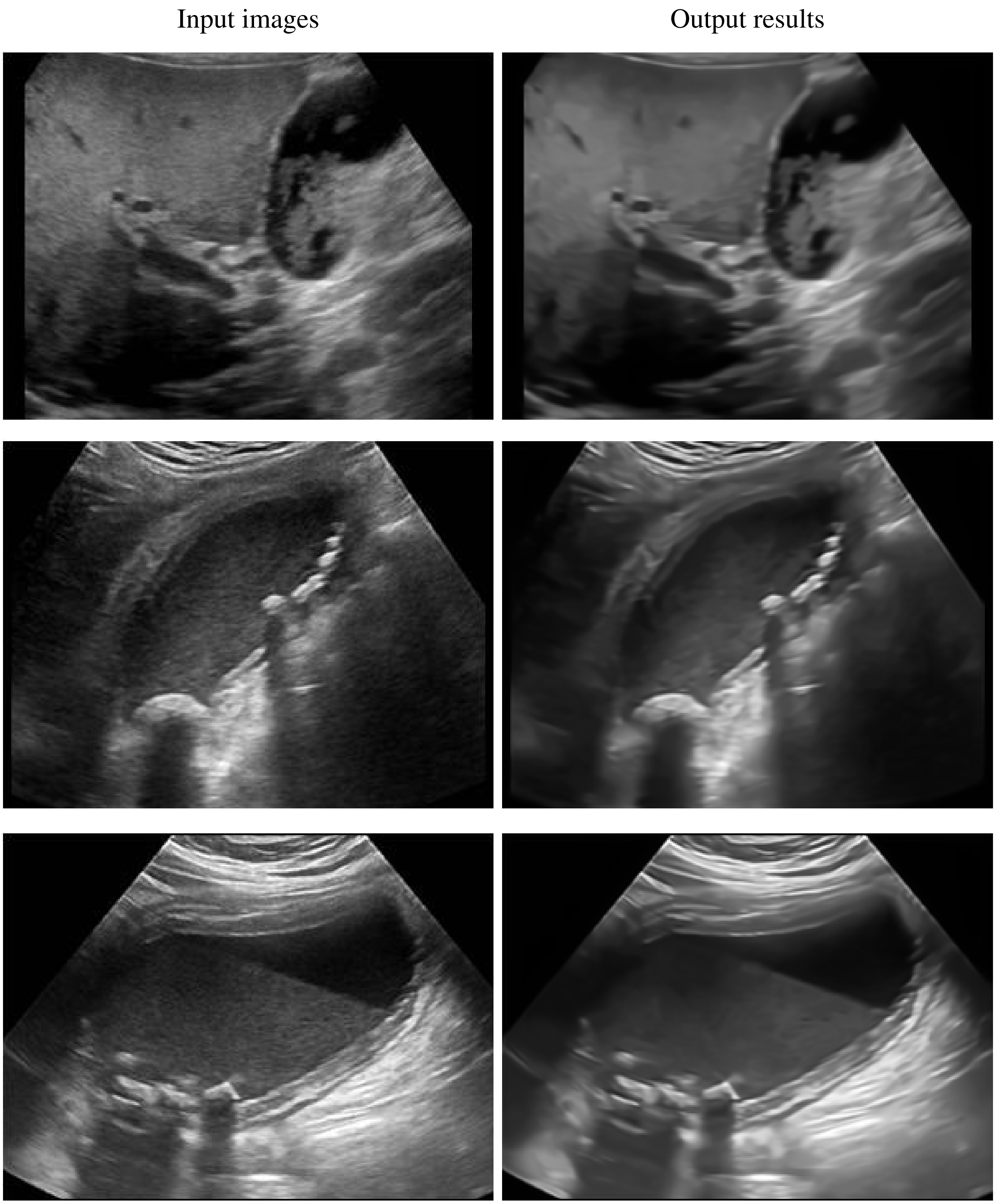

Figure 11: Additional ultrasound speckle reduction results produced from our method.

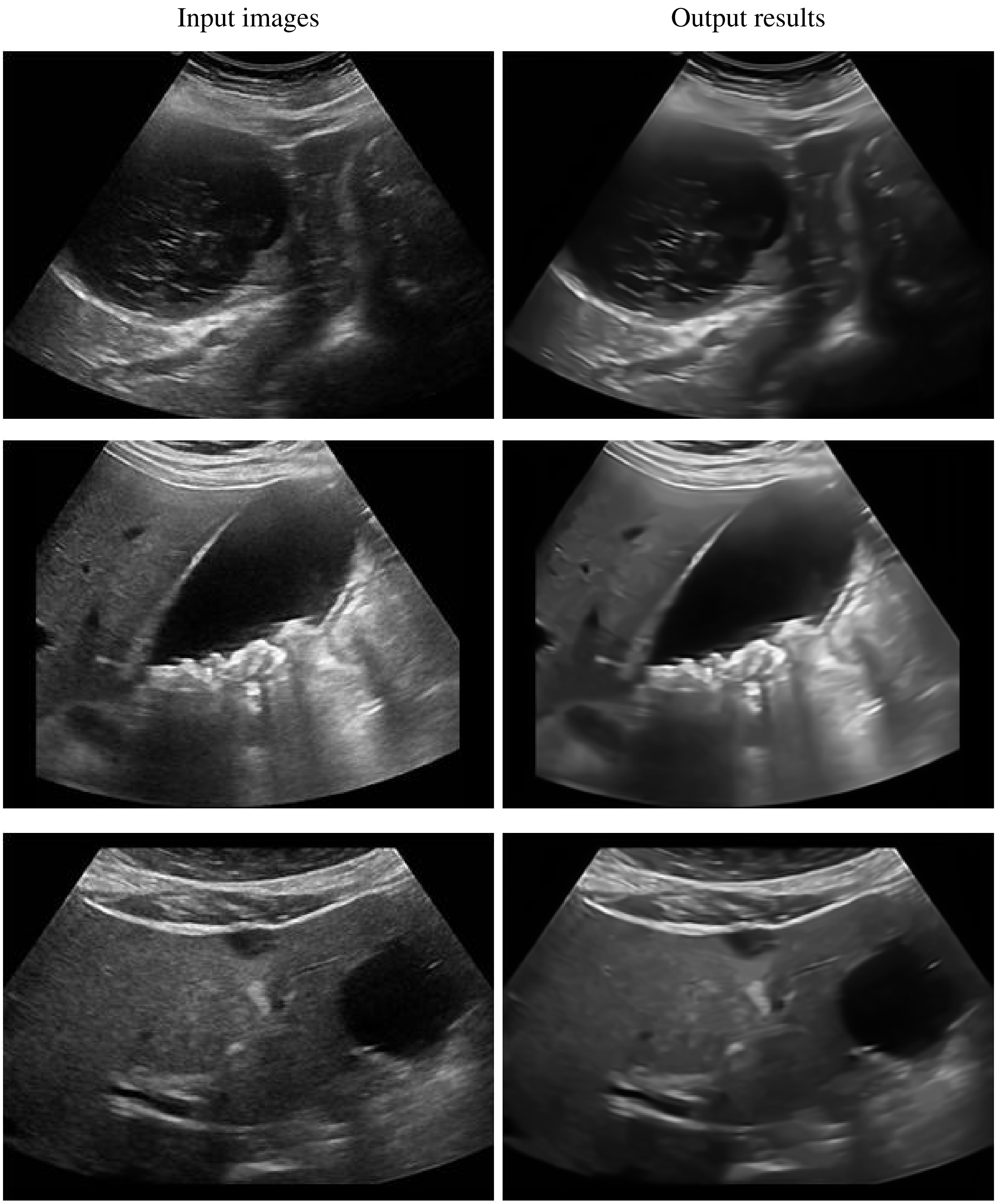

Figure 12: Additional ultrasound speckle reduction results produced from our method.

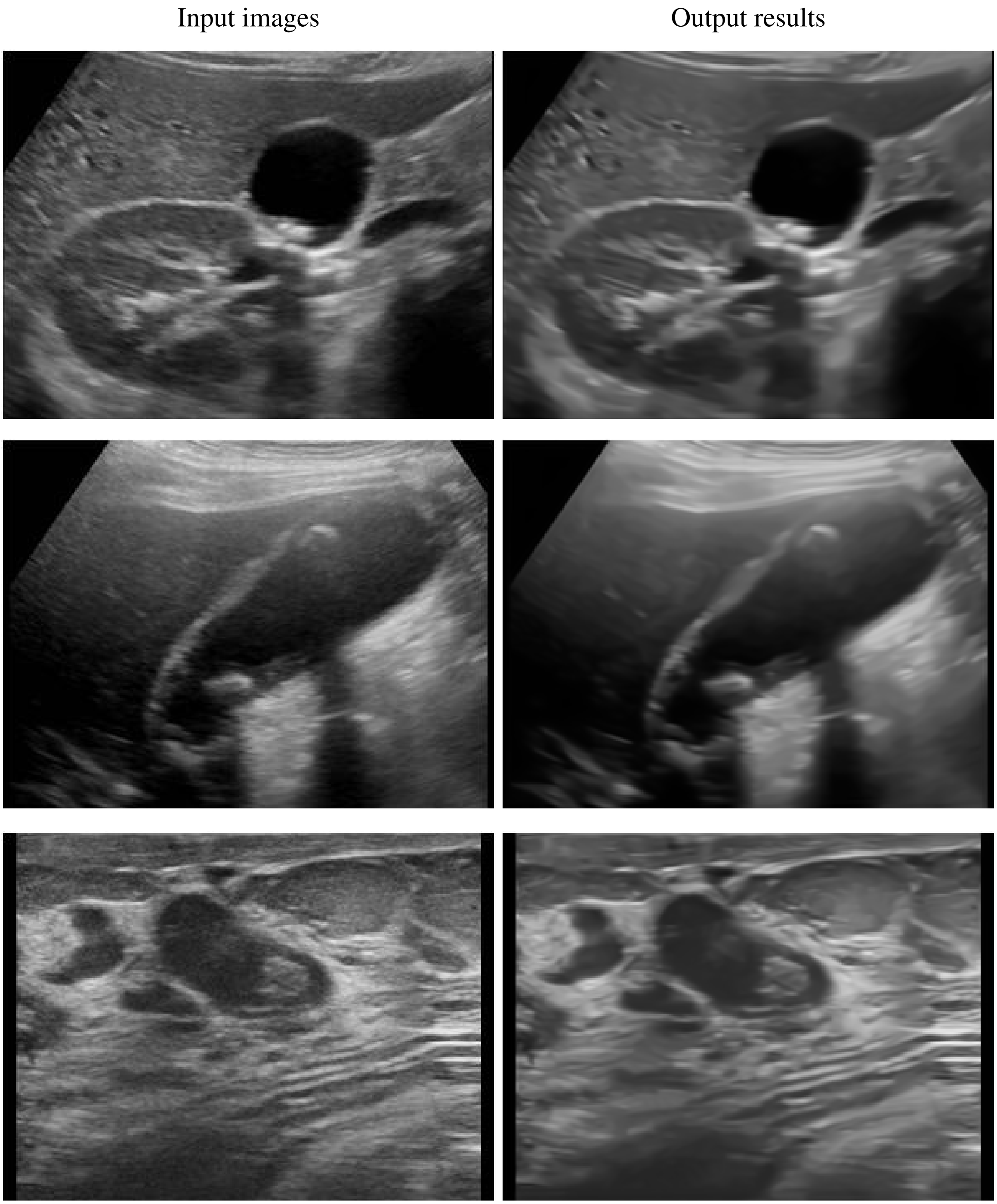

Figure 13: Additional ultrasound speckle reduction results produced from our method.

Input images | Output results

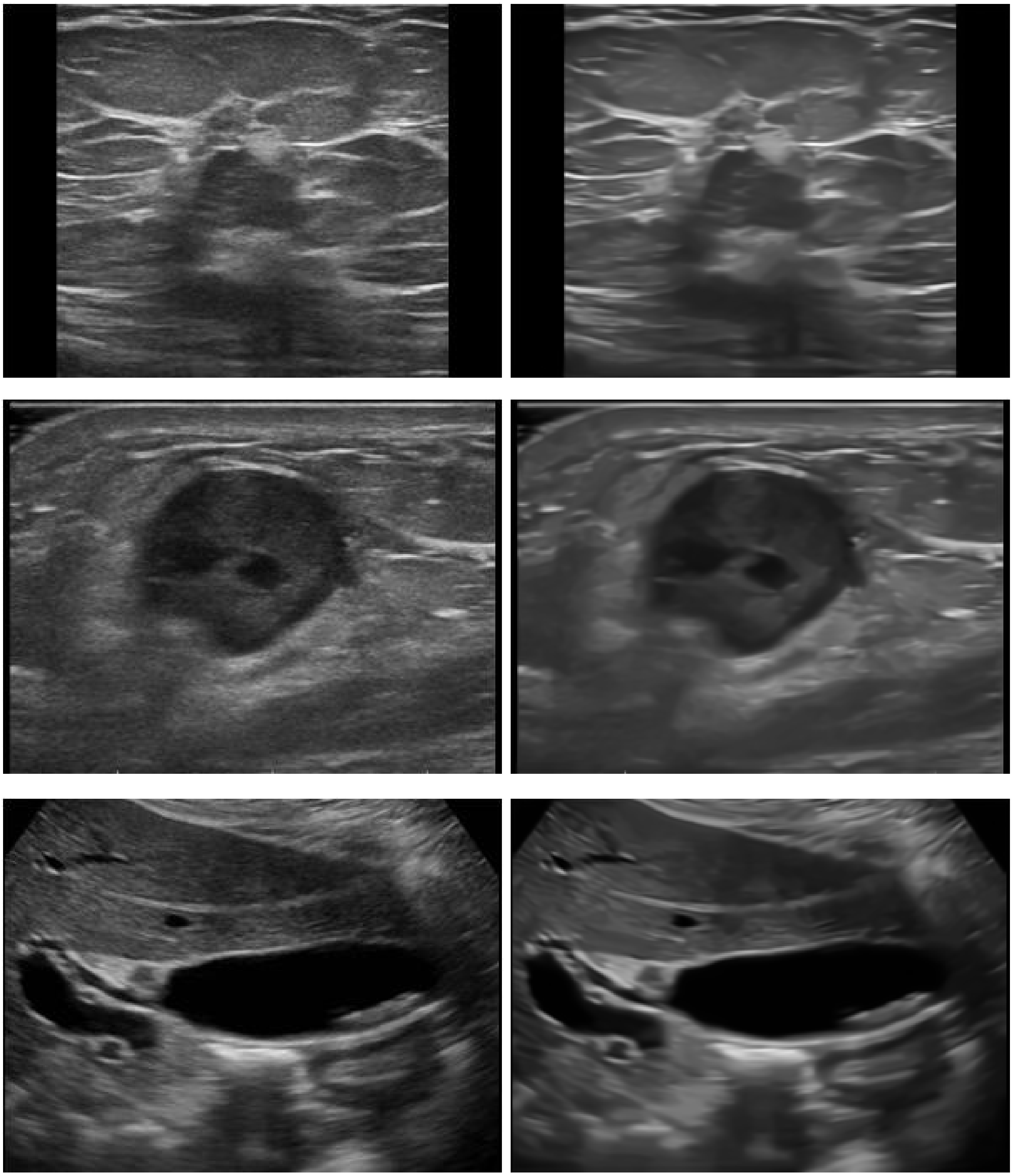

Figure 14: Additional ultrasound speckle reduction results produced from our method.

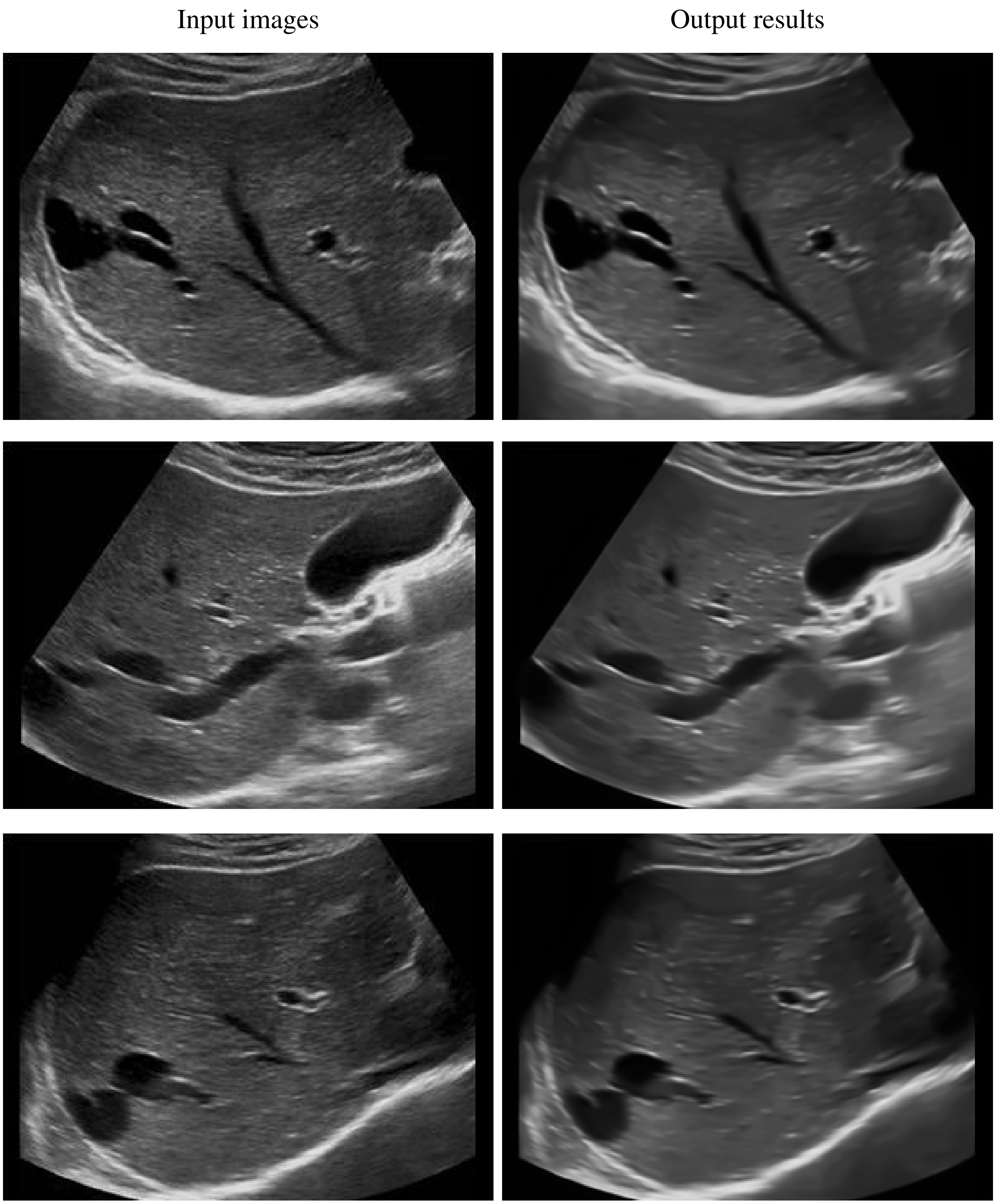

Figure 15: Additional ultrasound speckle reduction results produced from our method.

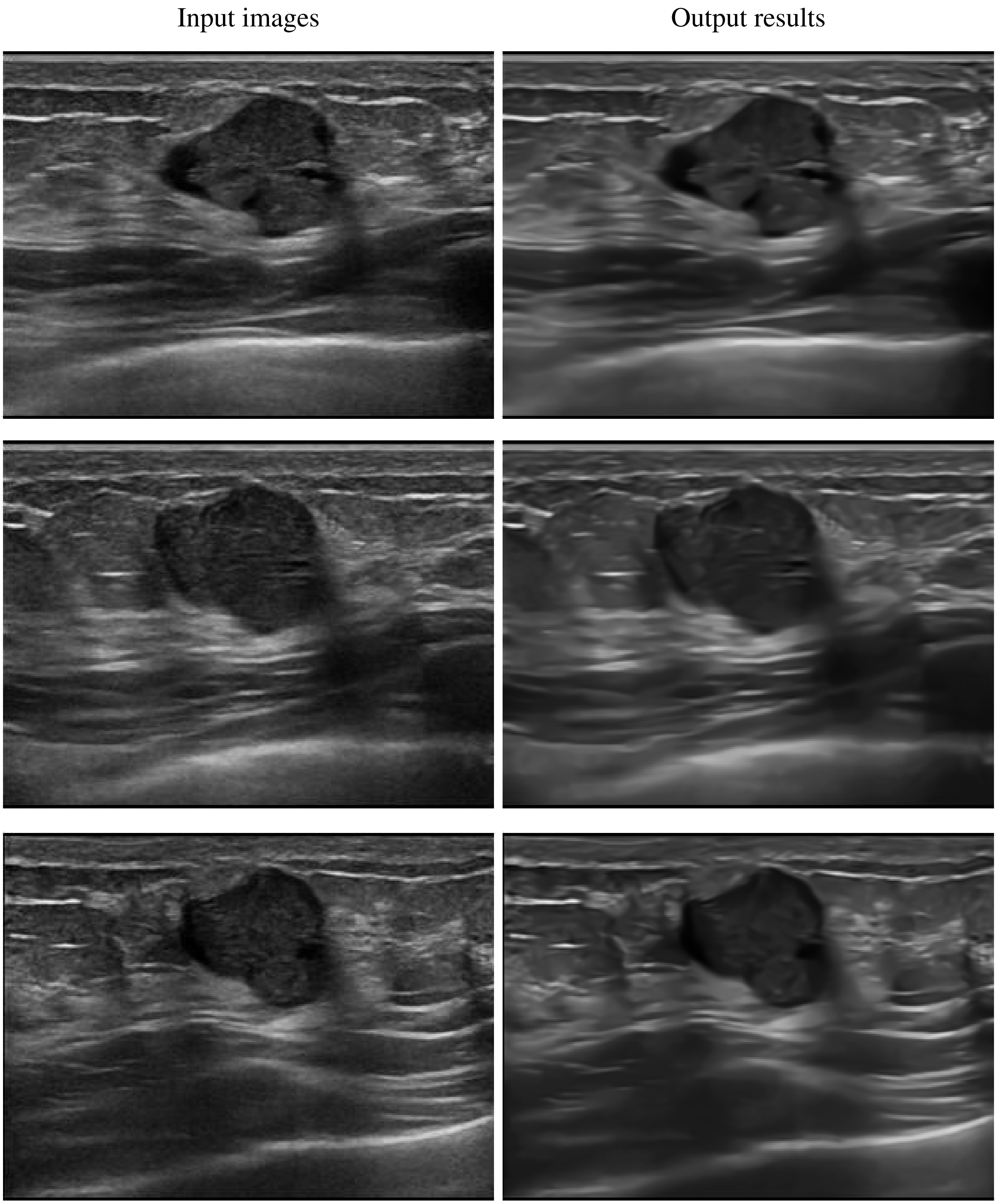

Figure 16: Additional ultrasound speckle reduction results produced from our method.

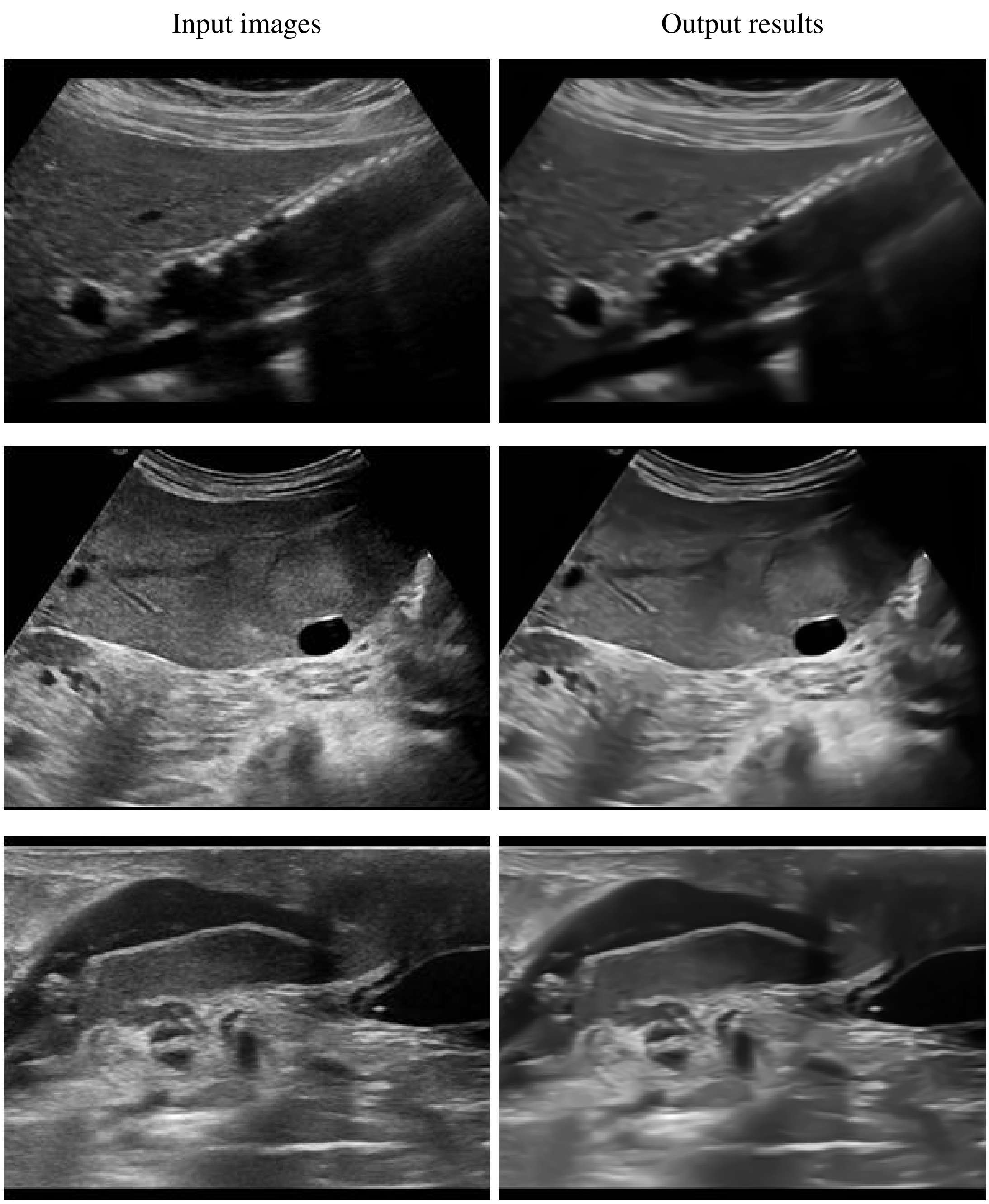

Figure 17: Additional ultrasound speckle reduction results produced from our method.

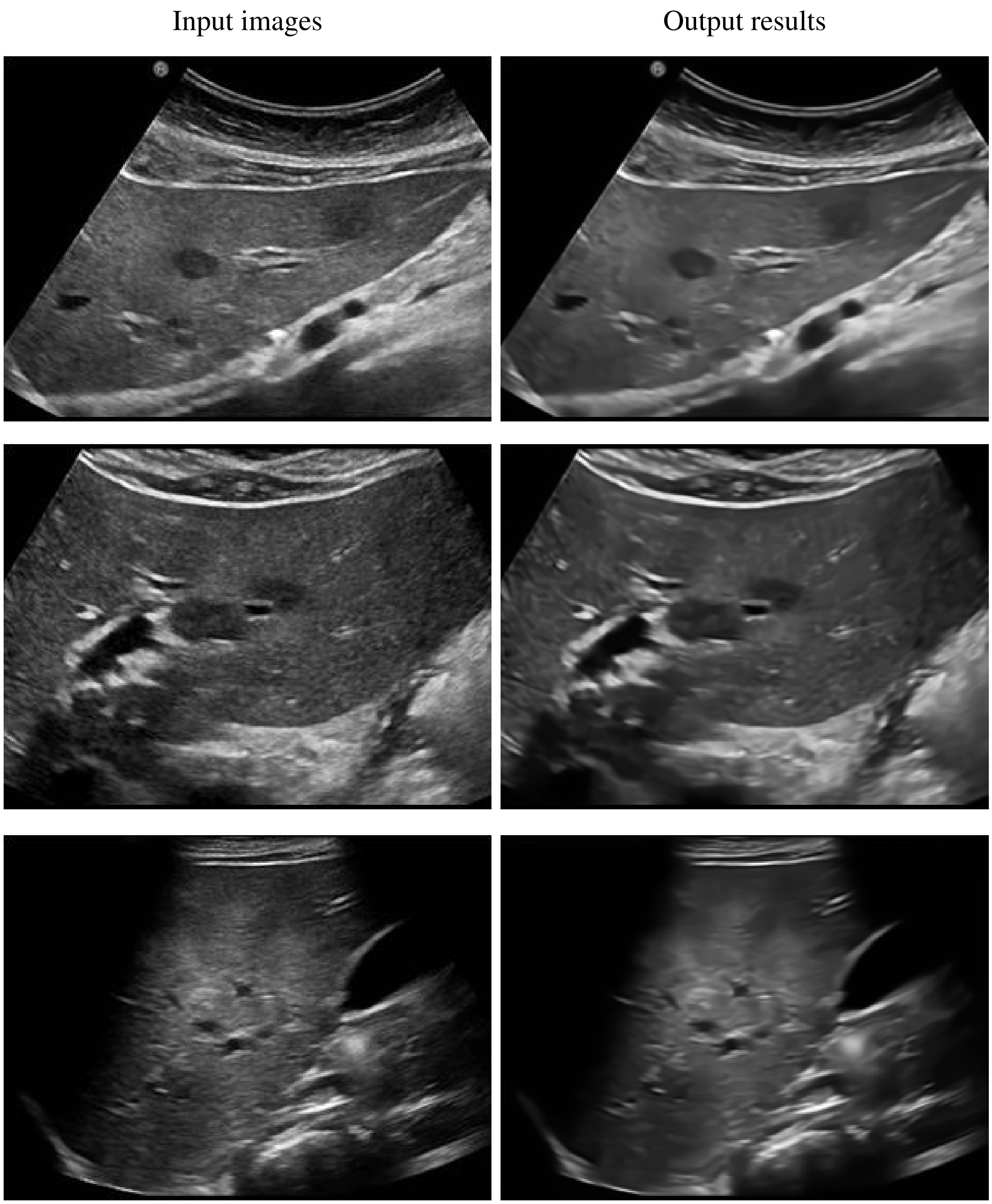

Figure 18: Additional ultrasound speckle reduction results produced from our method.

Input images Output results

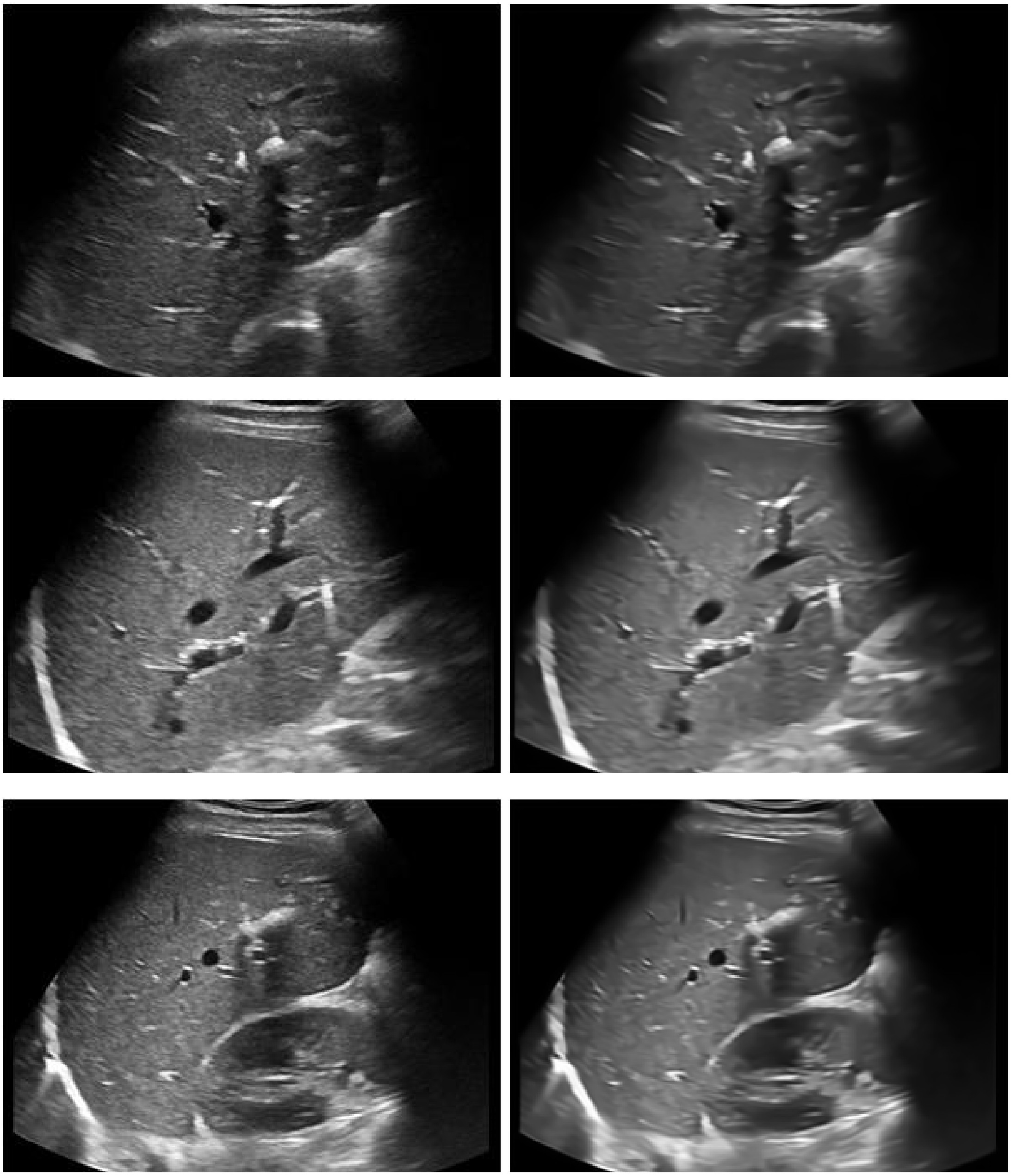

Figure 19: Additional ultrasound speckle reduction results produced from our method.

Input images Output results

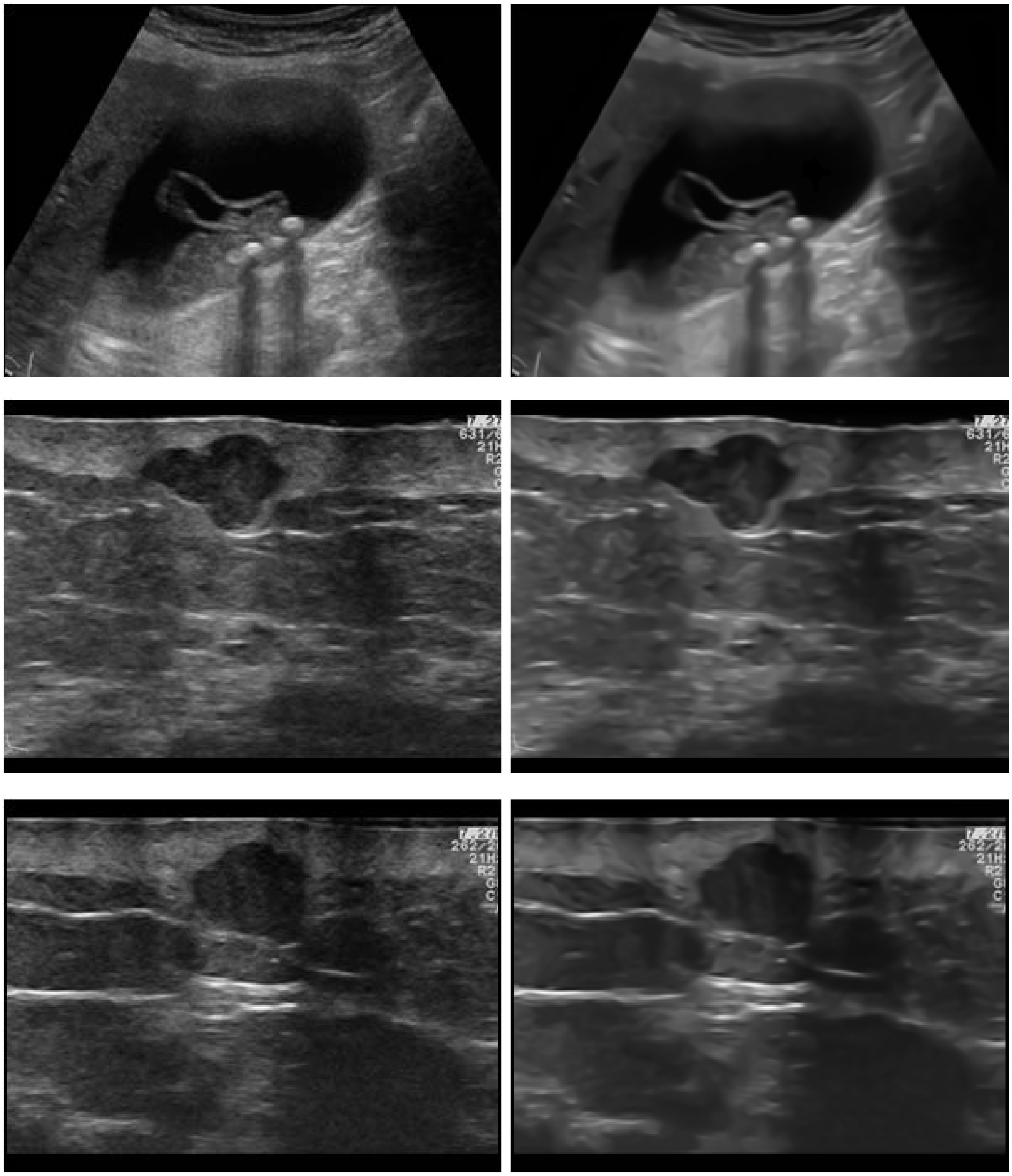

Figure 20: Additional ultrasound speckle reduction results produced from our method.

Part 4. Additional Segmentation results

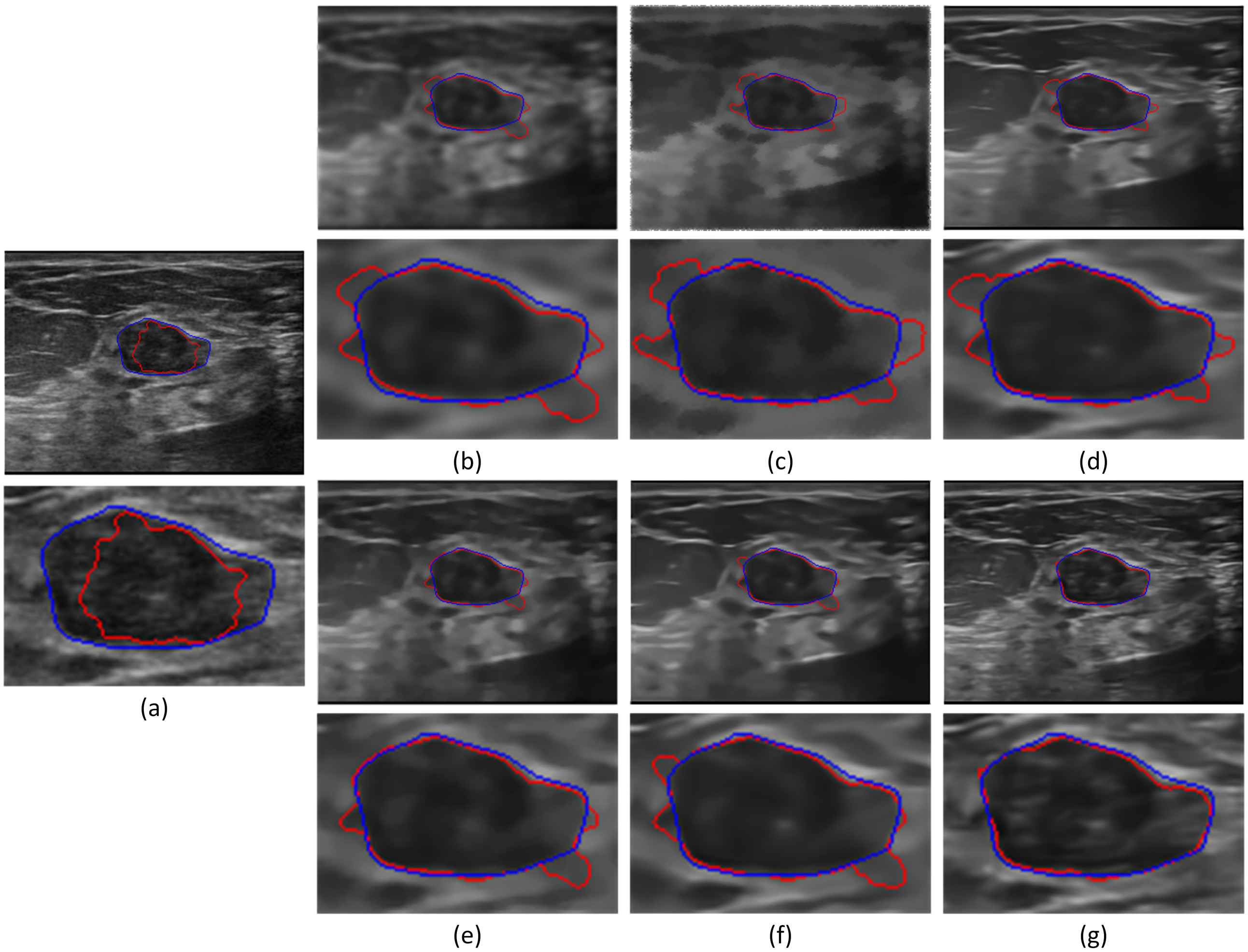

Figure 21: Additional segmentation comparison #1. (a) top row: segmentation result on the raw input breast ultrasound image with a benign fibroadenoma; bottom row: zoom-in view. Top row of (b)-(g): segmentation results on despeckled ultrasound images produced from SRAD [11], SBF [8], OBNLM [1], ADLG [2], NLMLS [10], and our method, respectively; bottom row of (b)-(g): associated zoom-in views. Blue color: the ground truth delineated by clinical doctors; and Red color: segmentation results produced on different inputs.

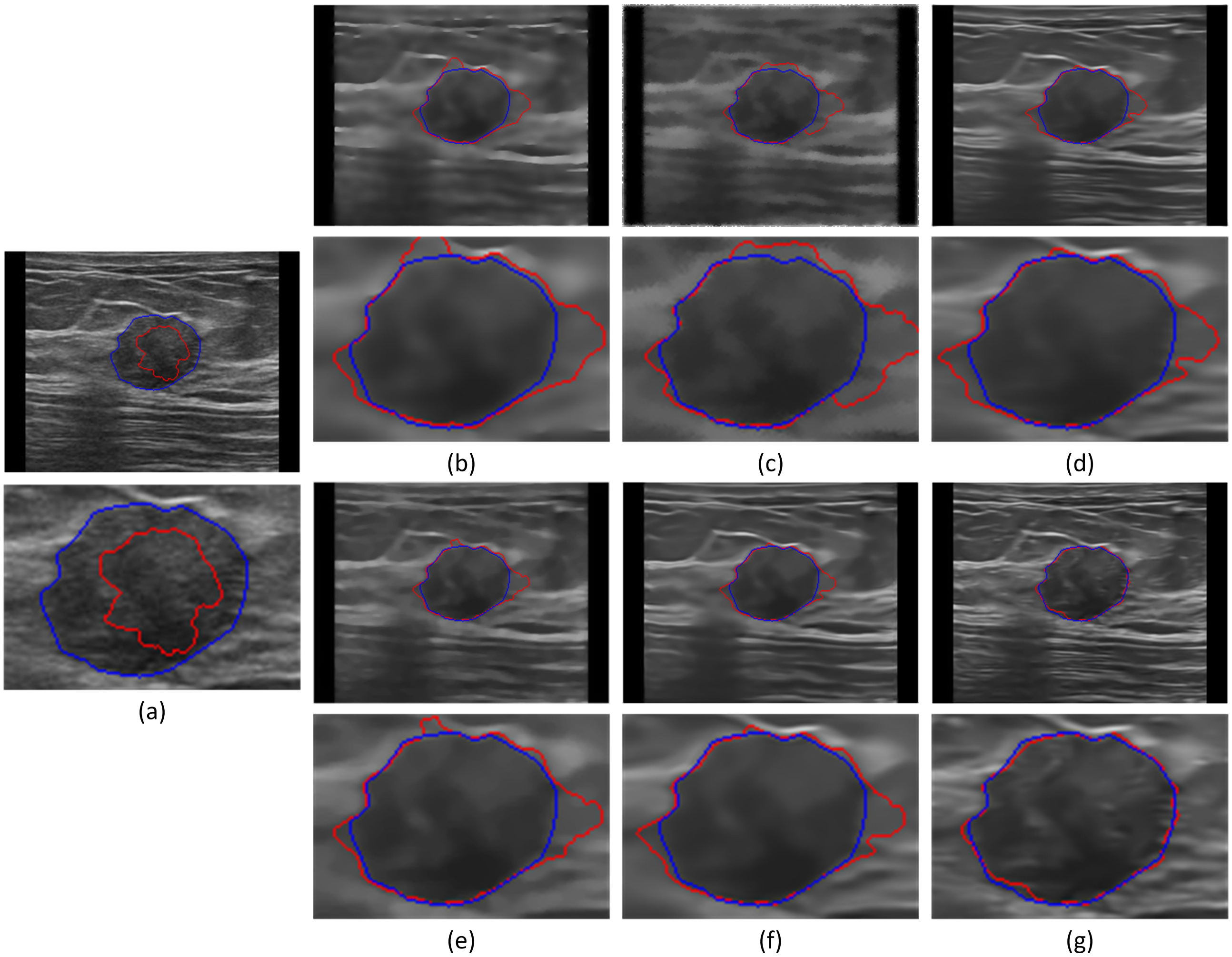

Figure 22: Additional segmentation comparison #2. (a) top row: segmentation result on the raw input breast ultrasound image with a carcinoma tumor; bottom row: zoom-in view. Top row of (b)-(g): segmentation results on despeckled ultrasound images produced from SRAD [11], SBF [8], OBNLM [1], ADLG [2], NLMLS [10], and our method, respectively; bottom row of (b)-(g): associated zoom-in views. Blue color: the ground truth delineated by clinical doctors; and Red color: segmentation results produced on different inputs.

References

[1] P. Coupé, P. Hellier, C. Kervrann, and C. Barillot. Nonlocal means-based speckle filtering for ultrasound images. *IEEE TIP*, 18(10):2221–2229, 2009. 9, 10, 11, 12, 13, 14, 15, 16, 17, 18, 29, 30

[2] W. G. Flores, W. C. de Albuquerque Pereira, and A. F. C. Infantosi. Breast ultrasound despeckling using anisotropic diffusion guided by texture descriptors. *Ultrasound in Medicine & Biology*, 40(11):2609–2621, 2014. 9, 10, 11, 12, 13, 14, 15, 16, 17, 18, 29, 30

[3] S. Gu, L. Zhang, W. Zuo, and X. Feng. Weighted nuclear norm minimization with application to image denoising. In *CVPR*, 2014. 7

[4] S. Ji and J. Ye. An accelerated gradient method for trace norm minimization. In *ICML*, pages 457–464. ACM, 2009. 7

[5] Z. Lin, M. Chen, and Y. Ma. The augmented lagrange multiplier method for exact recovery of corrupted low-rank matrices. *arXiv preprint arXiv:1009.5055*, 2010. 3

[6] Z. Lin, A. Ganesh, J. Wright, L. Wu, M. Chen, and Y. Ma. Fast convex optimization algorithms for exact recovery of a corrupted low-rank matrix. *Computational Advances in Multi-Sensor Adaptive Processing (CAMSAP)*, 61, 2009. 3

[7] J. Mairal, R. Jenatton, F. R. Bach, and G. R. Obozinski. Network flow algorithms for structured sparsity. In *NIPS*, 2010. 7, 8

[8] P. C. Tay, C. D. Garson, S. T. Acton, and J. A. Hossack. Ultrasound despeckling for contrast enhancement. *IEEE TIP*, 19(7):1847–1860, 2010. 9, 10, 11, 12, 13, 14, 15, 16, 17, 18, 29, 30

[9] J. Von Neumann. *Some matrix-inequalities and metrization of matric space*. 1937. 4

[10] J. Yang, J. Fan, D. Ai, X. Wang, Y. Zheng, S. Tang, and Y. Wang. Local statistics and non-local mean filter for speckle noise reduction in medical ultrasound image. *Neurocomputing*, 195:88–95, 2016. 9, 10, 11, 12, 13, 14, 15, 16, 17, 18, 29, 30

[11] Y. Yu and S. T. Acton. Speckle reducing anisotropic diffusion. *IEEE TIP*, 11(11):1260–1270, 2002. 9, 10, 11, 12, 13, 14, 15, 16, 17, 18, 29, 30

[12] D. Zhang, Y. Hu, J. Ye, X. Li, and X. He. Matrix completion by truncated nuclear norm regularization. In *CVPR*, 2012. 4, 5, 6, 7